PLOS Computational Biology

RESEARCH ARTICLE

Spatio–temporal modelling of *in vitro* influenza A virus infection: The impact of defective interfering particles on the type I interferon response

Yimei Li[1], **Bjarke Frost Nielsen**[2], **Simon A. Levin**[3], **Aartjan J.W. te Velthuis**[4*], **Bryan T. Grenfell**[3*]

1 Lewis-Sigler Institute for Integrative Genomics, Princeton University, Princeton, New Jersey, United States of America, **2** High Meadows Environmental Institute, Princeton University, Princeton, New Jersey, United States of America, **3** Department of Ecology and Evolutionary Biology, Princeton University, Princeton, New Jersey, United States of America, **4** Lewis Thomas Laboratory, Department of Molecular Biology, Princeton University, Princeton, New Jersey, United States of America

* aj.te.velthuis@princeton.edu (AJWTV), grenfell@princeton.edu (BTG)

OPEN ACCESS

Citation: Li Y, Nielsen BF, Levin SA, te Velthuis AJW, Grenfell BT (2026) Spatio–temporal modelling of *in vitro* influenza A virus infection: The impact of defective interfering particles on the type I interferon response. PLoS Comput Biol 22(4): e1014198. https://doi.org/10.1371/journal.pcbi.1014198

Editor: Peter M Kasson, Georgia Institute of Technology, UNITED STATES OF AMERICA

Received: December 9, 2025

Accepted: April 6, 2026

Published: April 22, 2026

Data availability statement: All simulation codes, analysis scripts, and data supporting the results of this study are openly available at: https://github.com/yimei-li/spatial-dynamics.

Funding: This manuscript is the result of funding in whole or in part by the National

Abstract

Defective interfering particles (DIPs) are incomplete viral genomes that modulate infection by competing with wild–type viruses and activating the innate immune response. Activation of the immune response leads to the production of cytokines and chemokines, including type I interferon (IFN), which restricts viral growth and may cause cell death. How DIPs interact with type I interferon (IFN) in spatially structured environments remains unclear. Focusing here on influenza A viruses, we developed a spatially explicit, stochastic model of *in vitro* viral infection that integrates virus and DIP replication, IFN signalling, and alternative dispersal modes. We find that: (1) our model captures the ring–like and patchy plaque morphologies observed experimentally; (2) IFN production peaks at an intermediate DIP ratio, reflecting a trade–off between early immune activation and sufficient co–infection; and (3) even a small fraction of long–range spread by virus and DIPs enables escape from the immune-based containment despite long-range IFN diffusion; this causes stronger antiviral responses but earlier peaks in virus egress at similar levels of cell loss. The model is available as an interactive platform: https://shiny-spatial-infection-app-production.up.railway.app/.

Author summary

Viruses such as influenza A virus, measles virus, and severe acute respiratory syndrome coronavirus 2 (SARS-CoV-2) often produce defective copies of their genomes during replication. These defective genomes cannot spread on their own without standard virus, but they interfere with viral growth and can trigger

Institutes of Health (NIH). It is subject to the NIH Public Access Policy. Through acceptance of this federal funding, NIH has been given a right to make this manuscript publicly available in PubMed Central upon the Official Date of Publication as defined by NIH. This work was supported by a Princeton Catalysis Initiative award (to B.T.G. and A.J.W.t.V.); Princeton Precision Health award (to B.T.G.); NIH grant DP2 AI175474 (to A.J.W.t.V.); the Carlsberg Foundation grants CF23-0173 and CF24-1337 (to B.F.N.); National Cancer Institute, NIH, Prime Contract No. 75N91019D00024, Task Order No. 75N91023F00016 (to Y.L.) (the content of this publication does not necessarily reflect the views or policies of the Department of Health and Human Services, nor does mention of trade names, commercial products or organizations imply endorsement by the U.S. Government); and the National Science Foundation (DMS-2327711, to Y.L., Collaborative Research: IHBEM: Data-driven multimodal methods for behavior-based epidemiological modeling). The funders had no role in study design, data collection and analysis, decision to publish, or preparation of the manuscript. No authors received a salary directly from any of the funders for this work. The content is the responsibility of the authors and does not represent the official view of the funding agencies.

Competing interests: The authors have declared that no competing interests exist.

strong immune responses. We were interested in understanding how the timing and location of these defective particles influence the immune system's ability to control viral infection. Infections do not spread evenly through the body—viruses and immune signals move locally, and some viruses may escape immune control. To study this, we developed a spatial simulation of a viral infection in a layer of cells. We found that if we allow for even a very small number of viral and defective viral particles to spread over longer distances, viruses can break through local immune barriers. We also visualize that producing more defective genomes does not always result in stronger immunity; instead, there is a balance between early immune activation and the ability of the infection to continue spreading. Our results help explain why infections vary in severity and suggest that defective genomes are a strategy for controlling viral diseases only at specific defective viral genome populations.

Introduction

Populations of RNA viruses, such as influenza A virus (IAV), are generally composed of both standard (or wild–type) and nonstandard viral particles. Nonstandard particles contain genomes that functionally differ from the wild–type. A special group of nonstandard particles is the defective interfering particles (DIPs) [1–3]. DIPs are virus–derived particles with incomplete or defective viral genomes (DVGs) that cannot replicate without co–infection with a standard virus (though coinfection of a cell by two DIPs with complementary genomes may in principle also support replication). DVGs with a smaller genome size, also called deletion–containing viral genomes (DelVGs), may replicate more quickly and outcompete standard viruses for host cell resources, while altered gene expression can yield proteins that interfere with standard virus protein function [3–6]. Despite these differences, DIPs co–exist and co–transmit with standard viruses in tissue culture as well as in humans, influencing infection spread and disease outcome by modulating viral adaptation, virulence, and immune evasion [3,5,7–11].

DIPs and IFN responses

An important way in which DIPs shape infection dynamics—particularly in IAV infection—is by triggering stronger innate immune responses [12,13]. Replication and transcription products derived from shortened DIP genomes are more potently detected by pattern recognition receptors (PRRs) such as retinoic acid–inducible gene I (RIG–I) than full–length wild type genomes [3,14,15]. Activation of these PRRs initiates signalling pathways that lead to expression of type I and III interferons (IFNs) and various pro–inflammatory cytokines, which are important for dendritic cell activation, fever, and shaping adaptive immunity [16], making DIPs critical actors in virus–host interactions [3]. DIPs have been shown to impact disease progression, act as antiviral and antitumour agents, and interfere with the efficacy of live attenuated

vaccines (e.g., IAV [17], measles [18], rubella [19], and others [20]). These features have renewed interest in quantitative understanding of how DIPs alter infection dynamics and innate immunity [9,21].

Limitations of existing models

Several computational studies have explored within–host *in vitro* infection dynamics, yet critical gaps remain in integrating spatial resolution, immune responses, and viral diversity. Traditional ordinary differential equation (ODE) models, which represent infection and immune processes as changes in average population densities over time, have assumed that IFN reduces viral production by infected cells, decreases the likelihood of infection, or renders uninfected cells refractory to infection [22–24]. However, such models lack spatial information and implicitly assume uniform IFN protection across the tissue, even in cases where DIPs are included [4,25]. A spatial framework for *in vitro* infection dynamics was introduced by Howat et al. [26], who developed a stochastic, spatially explicit computational model of IFN responses. However, their model assumed instantaneous and global IFN diffusion. Moreover, in the previous model, once triggered, IFN did not decline, and cells that transitioned to the antiviral state remained permanently antiviral. However, others have shown that negative feedback loops can suppress IFN production and potentially revert a cell to a non-antiviral state [27]. In addition, the assumed delay before this transition was very long (95 hours), and the model did not incorporate DIPs, thereby potentially overlooking gradients, gradual activation dynamics, and DIP–IFN interactions. Other models have examined DIP–virus interactions at intracellular or population levels but without immune components such as IFN signalling, limiting their applicability to immune–competent systems [28–32]. Akpinar et al. linked single–cell dynamics to plaque–level outcomes using a spatial cellular automaton, showing how spread depends on initial co–infection with viruses and DIPs [9]; Baltes *et al.* [33] directly visualised DIP–virus co–transmission, distinguishing virus–only, DIP–only, and co–infected cells through different fluorescent markers; and Liang *et al.* [34] analysed such plaque images using binarisation and geometric segmentation. While each of these studies highlighted the spatial structure of viral particles spreading, none incorporated IFN responses, leaving open how innate immunity modulates DIP–virus dynamics.

To bridge these gaps, we developed a stochastic, cell–based computational model of *in vitro* infection dynamics, incorporating DIPs, IFN signalling, and spatial structure (see Fig 1 and Fig A in S1 Appendix for a schematic representation). Our framework is designed to explore how DIP–virus interactions generate heterogeneous plaque structures, how different dispersal routes (cell–to–cell spread, finite–rate diffusion, or rare long–range jumps) influence infection dynamics, and how IFN signalling—whether instantaneous or finite–rate diffusion—modulates immune protection. Our model can naturally reproduce ring–like and patchy plaque morphologies, as observed experimentally. Together, these aspects highlight how spatial structure, viral diversity, and innate immunity combine to shape infection outcomes.

These multiple components are important because immune responses are inherently heterogeneous due to the structural complexity, diverse cell populations, and spatially varying microenvironments of human organs. For instance, in the lung, alveolar and bronchial regions exhibit distinct immune activities, with alveoli specialised for gas exchange and bronchi acting as physical barriers to infection [35–37]. Similarly, in the liver, during hepatitis B infection, the virus may exploit regions of low immune activity near central veins as “safe zones”, evading immune clearance and underscoring the need to include spatial and immune heterogeneity in infection models [38]. While *in vivo* complexity motivates the need for a more biologically refined and spatially granular infection model, *in vitro* systems provide a controlled setting to isolate and model key spatial–immune interactions, helping bridge the gap and guide future experiments.

Application to IAV

IAV is a highly contagious respiratory pathogen that causes seasonal epidemics and occasionally severe pandemics, providing a well–established system in which to study DIP–mediated modulation of infection [16,39]. We parameterised key infection and immune timing parameters—such as virus and DIP burst sizes, IFN delay, and IFN decay—using values derived from published IAV infection experiments [40,41] (these parameter choices are described in detail in the

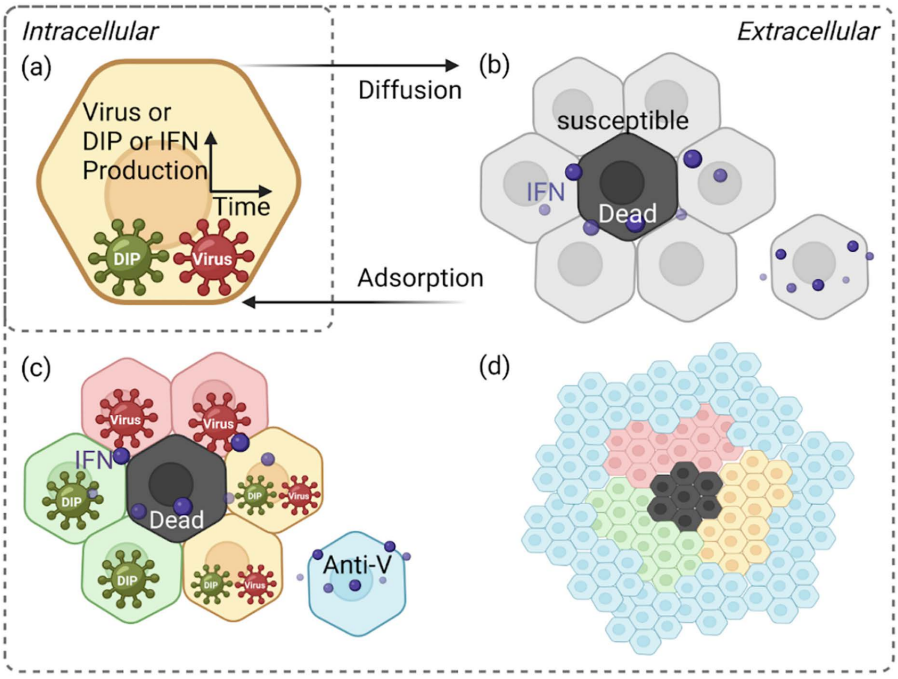

Fig 1. Schematic of the spatially explicit cell–based model. The model represents cell interactions and infection dynamics on a hexagonal lattice, capturing spatial organisation and simulating realistic cell–to–cell spread together with IFN effects. Particles are shown as dark green for DIPs and dark red for viruses. Cell states are colour–coded: light red for virus–infected cells, light green for DIP–infected cells, yellow for cells co–infected by both viruses and DIPs, black for dead cells, blue for antiviral cells, grey for susceptible cells, and purple dots represent interferon (IFN). **(a)** Intracellular stage: each infected cell produces viruses, DIPs, and IFN over time. **(b)** Initial infection: infected cells release viruses and DIPs. Infected cells ultimately undergo cell death, so releasing particles at cell death captures the overall outcome in the simulation. IFN spreads radially to nearby cells within a finite spatial radius on the hexagonal lattice. **(c)** Local spread: viruses infect neighbouring susceptible cells. **(d)** Antiviral state and recovery: dead cells are replaced through regrowth. Figure adapted from Howat et al. [26]. Created in BioRender. Li, **Y.** (2026) https://BioRender.com/3i0o6bk.

https://doi.org/10.1371/journal.pcbi.1014198.g001

Methods section). With these values, our model captures the interaction between viral diversity and IFN under biologically grounded conditions. During replication, IAV DIPs arise from internal deletions in one of the virus's eight RNA genome segments due to polymerase template switching. These DelVGs are typically 300–500 nt long, retaining 200 nt from each end of the full–length segment, which ranges from 890 nt (NS) to 2,341 nt (PB1/PB2) in length [42]. They serve as replication templates and are packaged into viruses, with most (in IAV) originating from polymerase–encoding segments [43,44].

Motivating questions

How does IFN spatial behaviour change under different diffusion assumptions—instantaneous versus finite–rate—and how does this influence immune protection? What happens if viruses, including DIPs, are not well–mixed, with some spreading across longer distances (e.g., influenced by convection, cilia movement, or virus particle shape [45]; we will call this "jumping" for simplicity) and generating infection patterns and innate immune responses akin to mucus–mediated dispersal in the respiratory tract? Is a larger DIP output always associated with a stronger IFN response? How do plaque dynamics—such as timing, peak virulence, and infected area—change with or without DIPs or IFN? How can we explain diverse plaque morphologies observed experimentally, including patchy structures, within a unified spatial–immune framework? These questions can be explored using our flexible online RShiny app, which allows users to visualise viral spread, IFN diffusion, and particle movement through dynamic videos; generate time series plots of cell states, virus counts, and

IFN levels; and analyse how outcomes vary across different parameter settings (https://shiny-spatial-infection-app-production.up.railway.app/).

Results

Model calibration

Calibration with DIP data in the absence of IFN. We first included DIPs and disabled IFN signalling to calibrate our model, following the experimental conditions of Baltes *et al.* [33], who engineered fluorescently labelled DIPs of vesicular stomatitis virus (VSV). Fig 2 compares experimental data with simulation outputs under matched inoculation (DIP–green fluorescent protein (GFP) input of 1) and field size.

To enable cell–by–cell quantification, the experimental image at 25 hours post-infection (hpi) (left) was pre–processed by tessellating the field into hexagonal cells and applying automated colour classification. This procedure identifies infection states (virus only, DIP only, or co–infected) even when colours are too faint to be distinguished by eye, yielding a representation from which the number of cells in each category can be counted. The resulting processed image (centre) forms the basis for quantitative comparison with the surrounding six stochastic replicates generated under a fixed parameter set (see Methods for details of parameter calibration).

Parameter values were estimated by scanning plausible ranges for virus and DIP spread (7–35 cells) and burst sizes (50–300 particles per lytic event). Each parameter combination was simulated 30 times, and averages were compared

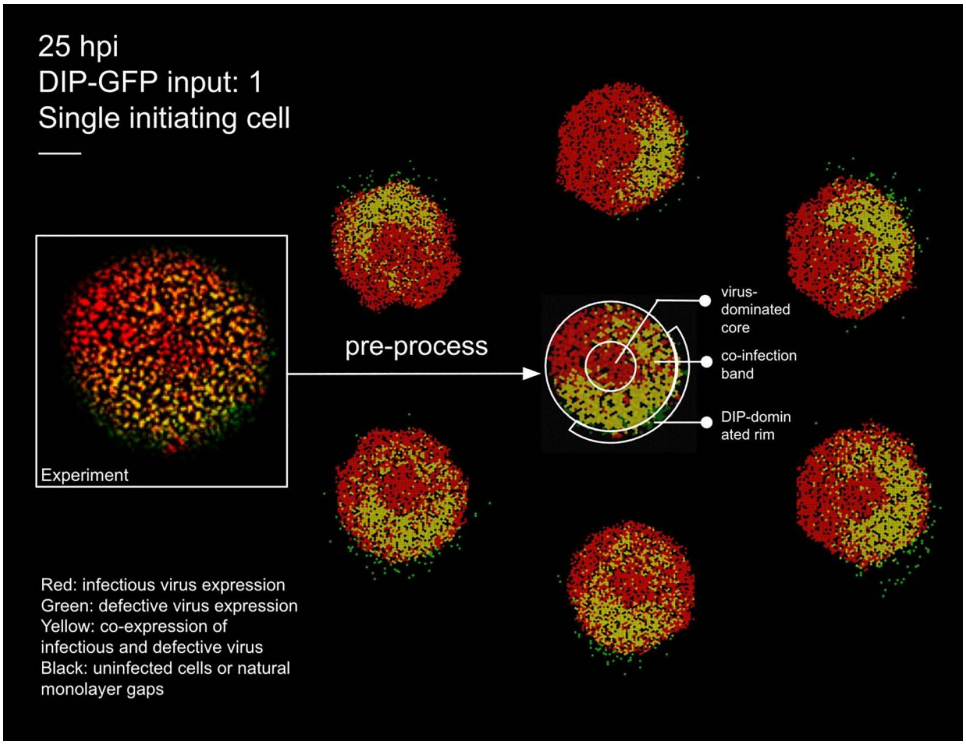

Fig 2. Experimental plaque and matched stochastic simulations at 25 hpi. Left: raw experimental image from [33] with DIP–GFP input of 1 (single initiating cell). Centre: pre–processed experimental image obtained by tessellating into hexagonal cells and applying automated colour classification, which resolves cell states even when colours are too faint to be distinguished by eye. This processed representation is used to count the number of cells in each state for quantitative comparison with simulations. Surrounding six panels: stochastic realisations under matched inoculation and field size, illustrating variability across runs. Colours: black, susceptible; red, virus–infected; green, DIP–infected; yellow, co–infected. Scale bar: 0.5 mm.

https://doi.org/10.1371/journal.pcbi.1014198.g002

to experimental counts of virus–only, DIP–only, and co–infected cells. The best-fitting set (minimising the discrepancy between simulated and experimental cell counts across all three infection classes; see Table A in S1 Appendix for the selected parameter values) was selected for subsequent analyses.

Ring–like and patchy structures emerge in the absence of IFN. Our model reproduces the ring–like and patchy plaque morphologies observed experimentally (see Methods and Table A in S1 Appendix for parameter values). These features arise naturally from particle–level stochastic dynamics, without requiring image binarisation or geometric segmentation as in other approaches [34]. Fig 2 illustrates this comparison: the left panel shows the experimental image, the centre panel the pre–processed tessellated representation, and the surrounding six panels representative stochastic simulations.

The central circular region is initially dominated by virus–infected cells (red). Due to the use of maximum–intensity projection, as in the experiment [33], the red signal persists for an extended period, reflecting the long half–life of red fluorescent protein (RFP)/GFP even after lysis and the presence of dead cells in the centre. In one sector of the advancing front, DIPs randomly seed a neighbouring region (green). Where these fronts overlap, a circumferential co–infected band appears (yellow).

The band is annular rather than a local patch, because the central red signal persists under maximum–intensity projection even after virus egress; the overlap therefore wraps around the circular core. An outer green rim forms because DIPs disperse farther than viruses. This mechanism explains the rings in Fig 2 and is consistent with the concentric–ring analysis and localised enrichment described in the experiment [33].

Beyond morphology, the model also captures the temporal dynamics of infection classes (Fig 3). Although variability across stochastic replicates is wide (grey 95% confidence intervals), the mean trajectories closely follow experimental trends, supporting the model's ability to reproduce both spatial and temporal aspects of DIP–virus interactions. The main discrepancies arise from stochasticity in whether initial DIP foci encounter virus and establish coinfection. When coinfection occurs early, both viruses and DIPs generate large bursts of progeny and sustain spread; when DIPs fail to meet virus, they quickly fade because they cannot replicate on their own.

Calibration with IFN responses in the absence of DIPs. After calibrating spatial heterogeneity using the Baltes *et al.* [33] dataset, we next validated IFN–mediated responses using the experiments of Howat *et al.* [26], who analysed Herpes simplex virus 1 (HSV–1) infections in Madin-Darby bovine kidney (MDBK) (IFN–competent) and Vero (IFN–deficient) cells [26,46–49]. As their model uses an antiviral delay and effective infection terms rather than explicit IFN or virus half–life parameters, we likewise did not estimate separate IFN or virus half–life terms in this calibration step. We set the antiviral delay time to 95 h, consistent with Howat *et al.* [26], which ensured that our framework captured IFN activation kinetics (Fig 4; see Methods and Table B in S1 Appendix for parameter values), providing support for the model framework, with good agreement with the experimental data.

Dynamics of the full DIP–IFN model

From calibration to IAV simulations. Together, these complementary calibration datasets—VSV with DIPs in the absence of IFN (Baltes *et al.* [33]), and HSV with IFN in the absence of DIPs (Howat *et al.* [26])—provide independent validation of our framework. Although obtained in different viral systems, they establish spatial and immune benchmarks that we used to parameterise subsequent simulations of IAV, the focus of this study (see Table C in S1 Appendix for parameter values; non–influenza-specific parameters follow those of the Baccam *et al.* within-host model [22]).

Exploration of IFN responses and dispersal modes. To examine how IFN dynamics shape infection outcomes, we varied three factors in all combinations: IFN response mode, particle movement, and composition. In Fig B in S1 Appendix, rows correspond to IFN mode (1 and 4: no IFN; 2 and 5: finite–range; 3 and 6: global/instantaneous), while columns correspond to particle movement (1: cell–to–cell; 2: finite–radius jumps; 3: random long–range jumps). The figure is also divided by composition: the top three rows show viruses with DIPs, whereas the bottom three rows show

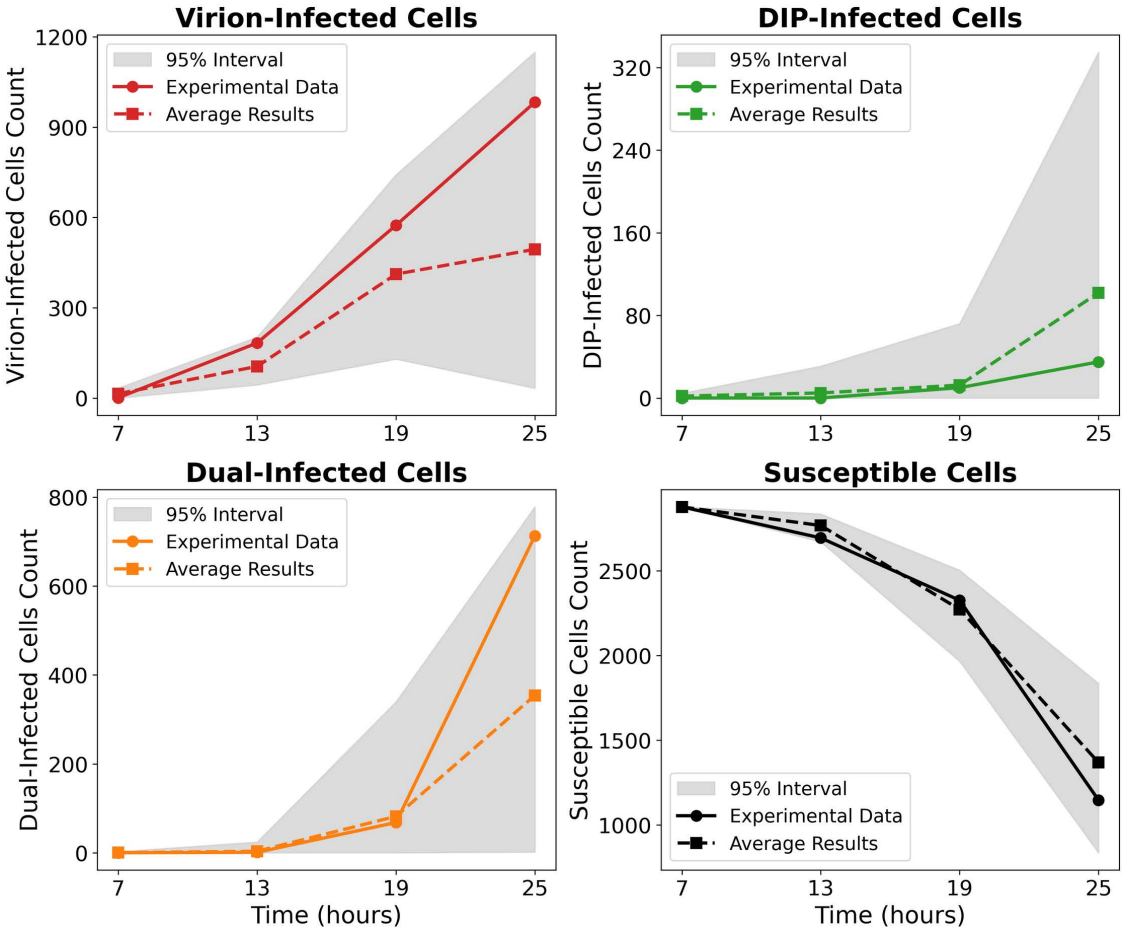

Fig 3. Model validation against experimental data from [33] in the absence of IFN. Cell counts are shown on a logarithmic scale for (top left) virion–infected cells, (top right) DIP–infected cells, (bottom left) co–infected cells, and (bottom right) susceptible cells at four time points (7, 13, 19, and 25 hpi). Solid lines represent experimental data, dashed lines show the mean of stochastic simulations with identical parameters, and grey shading indicates the 95% interval across these simulations.

https://doi.org/10.1371/journal.pcbi.1014198.g003

viruses only. The left panels display temporal changes in cell states and IFN levels, and the right panels show final plaque morphology. These simulations provide a systematic overview of model behaviour and establish a framework for later comparisons (see Fig B in S1 Appendix).

Emergent properties of the full model

Intermediate relative DIP yield maximises peak IFN. To investigate how variation in DIP production affects the spatial dynamics of IFN activation, we varied the *relative DIP yield* $Y^{\text{rel}}_{\text{DIP}}$, defined as the DIP:virus output ratio upon lysis of a virus–infected cell. In our model, $Y^{\text{rel}}_{\text{DIP}}$ ranged from 2 to 32, corresponding to DIP burst sizes of 100–1600 PFU/cell, assuming a fixed virus burst size of 50 PFU/cell based on experimental data and the baseline model [22]. We implemented global IFN signalling and restricted virus dispersal to cell–to–cell spread, using parameter values consistent with previous studies [46,50,51]. Simulations were run for 500 hours, with hourly measurements of plaque size, IFN concentration, and infection composition.

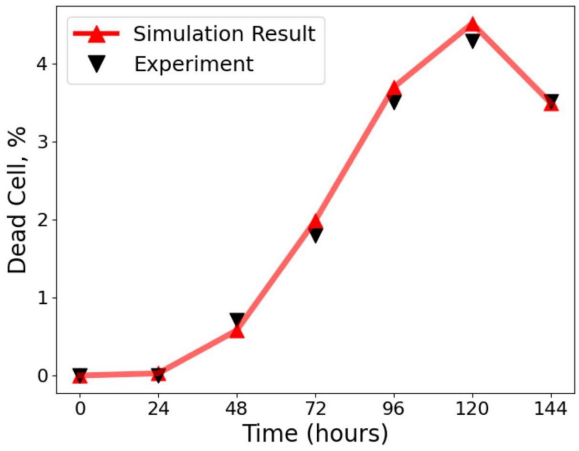

Fig 4. Comparison of model simulations with experimental data from Howat et al. [26]. The percentage of dead cells over time is shown, with simulation outputs (red line, triangles) closely matching experimental measurements (black triangles). Simulations used a time step of 1 h, and the virion infection probability was re–fitted to account for the susceptibility of MDBK cells to HSV infection, giving parameter estimates $\rho = 0.09$ [0.07, 0.11], $\tau = 95$ [88, 101] h, and $\alpha = 1.5$ [1.2, 1.8]. Experiments were initiated with an inoculum of 50 plaque-forming units (PFU), where the PFU represents a statistical average of plaques expected across repeated assays. Each simulation curve represents the mean of 30 independent realisations. This validates the parameterisation of our framework against the dataset of Howat et al. [26].

https://doi.org/10.1371/journal.pcbi.1014198.g004

We observed a nonmonotonic relationship between Y_{DIP}^{rel} and the IFN response, with a clear peak at an intermediate value of Y_{DIP}^{rel}, where the IFN concentration reached its maximum (Fig 5, left panel). Beyond this point, further increases in DIP output led to diminished IFN activation. This critical value coincided with the highest number of cells co–infected by both viruses and DIPs, which in our model are the strongest IFN producers—releasing ten times more IFN than virus–only infected cells and twice as much as DIP–only infected cells. At this yield, the virus–only infected population was minimal, while DIP–only infections were widespread. This configuration promoted efficient DIP dissemination, followed by sufficient virus co–infection to generate a large number of double–infected cells.

To make sure that the observed nonmonotone optimum is not a random outcome of stochastic variability, we further analysed replicate simulations using GAMs with 95% confidence interval and LOESS smoothing (Fig 5, right panel). Both methods consistently recovered an interior maximum in peak IFN across the explored values of the Y_{DIP}^{rel}. The exact location of this maximum may shift with the spline dimension and smoothness penalty, but the qualitative pattern is robust: peak IFN is highest at intermediate Y_{DIP}^{rel}, rather than increasing monotonically with Y_{DIP}^{rel}.

We obtained a similar result under a continuous Gaussian release formulation (Fig E in S1 Appendix): peak IFN still occurred at an intermediate relative DIP yield rather than at the scanned extremes. However, under continuous release, the IFN–yield curve could show additional fine structure, for example a small low-yield shoulder, a local maximum, or a less clearly defined peak, depending on the release-distribution parameters and the number of replicates per condition. Our supplementary analysis suggests that this is likely related to changes in the timing and extent of virus–DIP co-infection over time, while the main pattern remains unchanged. Additional details are provided in the Supplementary Information and in the GitHub repository.

The observed peak arises from the balance between two opposing regimes (Fig 5):

(1) At low Y_{DIP}^{rel}, DIP production was insufficient to support widespread DIP–only infections or effective co–infection. Consequently, the number of double–infected cells remained low, and total IFN output stayed limited despite virus spread.

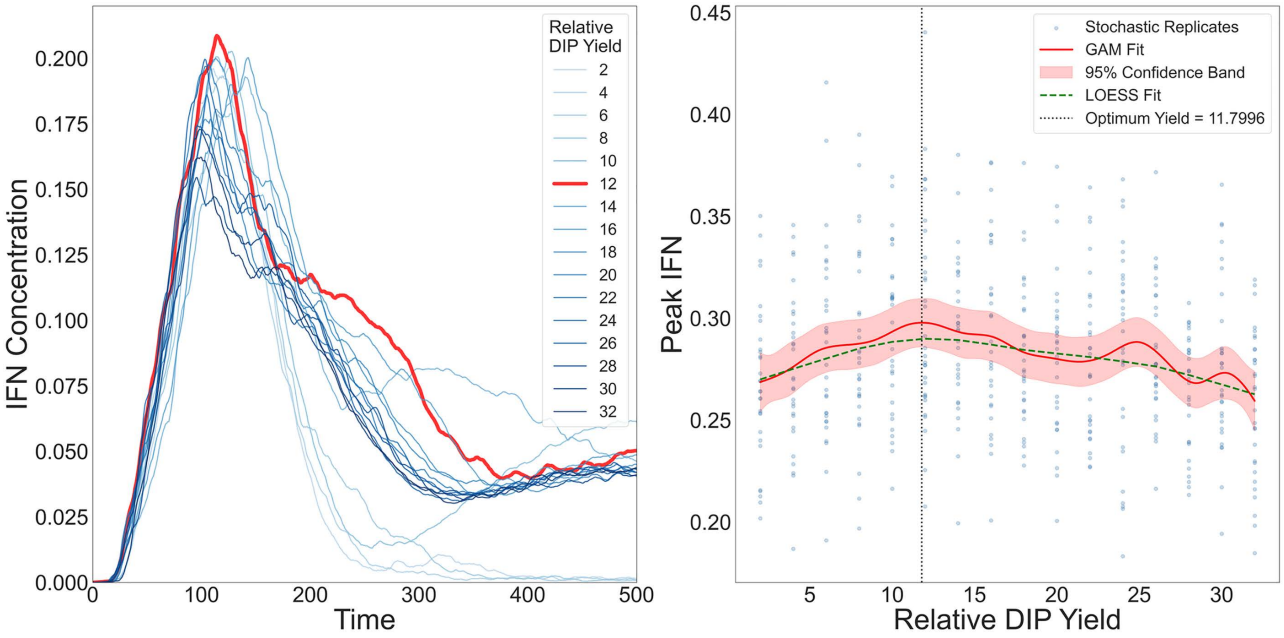

Fig 5. IFN dynamics across values of the relative DIP yield Y^{rel}_{DIP}. Left: IFN time series for increasing Y^{rel}_{DIP} . The response rises and then declines, with a maximum at approximately $Y^{rel}_{DIP} \approx 12$ (thick red trace). **Right:** Peak IFN versus Y^{rel}_{DIP} across stochastic replicates. Blue points show replicates. The generalised additive model (GAM) fit (red, with 95% confidence band) and the LOESS fit (green, dashed) agree on a non-monotone pattern with an intermediate optimum (vertical dotted line). Simulation times reflect plaque expansion in an idealised *in vitro* epithelial monolayer.

https://doi.org/10.1371/journal.pcbi.1014198.g005

(2) At high Y^{rel}_{DIP} , DIPs spread rapidly, initiating early co–infection and triggering early IFN release. Due to the exponential sensitivity of infection probability $P_{infection}$ to IFN levels, both DIPs and viruses quickly lost the ability to infect new cells, curtailing further spread and reducing cumulative IFN production.

Thus, an intermediate peak value of Y^{rel}_{DIP} marks the most effective balance between particle production, co–infection timing, and IFN–mediated feedback. Values above or below this point disrupt the coordination between DIP seeding and virus co–infection, ultimately leading to reduced IFN activation.

Minimal fractions of free–jump particles strongly enhance spread

To assess sensitivity to long–range transmission (e.g., mucus–mediated dispersal), we simulated infections with free–jump fractions from 1% to 90% in the absence of IFN; the remaining transmission occurred by cell–to–cell spread. As shown in Fig C in S1 Appendix (top left), even 1% free jumps accelerated plaque expansion and altered morphology, with satellite plaques visible by $t = 150$ h.

Under global IFN signalling, free jumps had little effect because uniform antiviral activation removed any advantage of escaping local immune zones (Fig C in S1 Appendix). In contrast, under local IFN signalling, even 1% free jumps had a strong impact.

Fig 6 shows these outcomes in detail. Despite an earlier and higher antiviral fraction with 1% free jumps (blue curves) than with no jumps (cyan), the dead–cell fraction (red curves) spikes much earlier and reaches peaks comparable to the no–jump IFN range 10 condition (orange). The reason is the response delay τ : free jumps establish foci beyond the contemporaneous IFN front, allowing damage to accumulate before local antiviral containment is established.

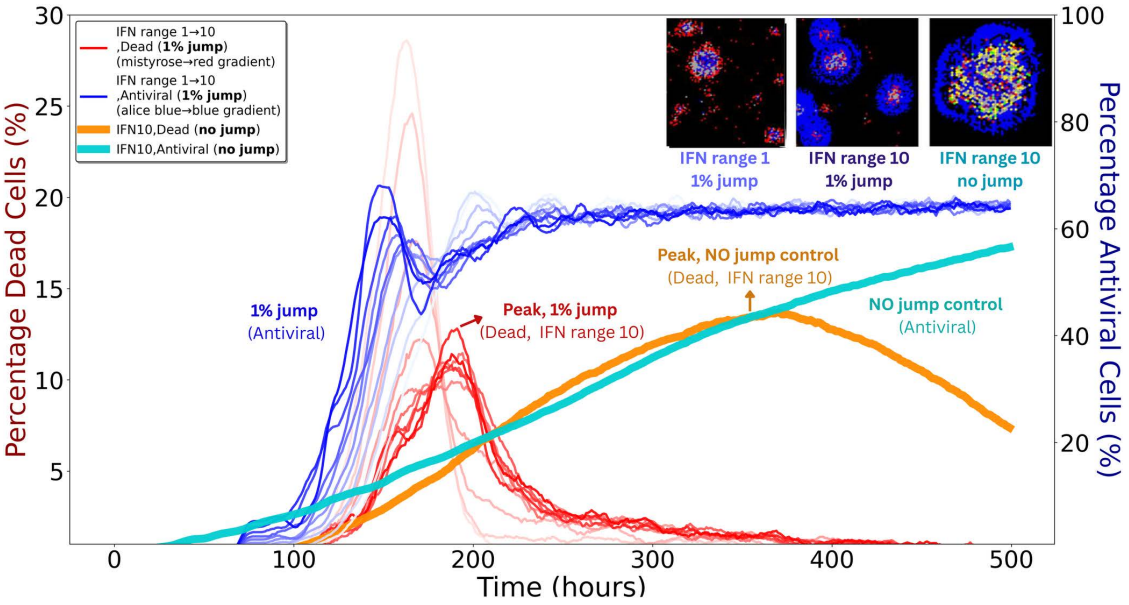

Fig 6. IFN range and spreading mode jointly shape plaque dynamics. Thin red and blue curves denote simulations with 1% free–jump transmission for both viruses and DIPs (remaining 99% cell–to–cell). Red gradients (left *y*–axis) show dead–cell fractions for IFN ranges 1–10, where free jumps generate earlier and higher peaks (arrow, "Peak, 1% jump"). Blue gradients (right *y*–axis) show antiviral–cell fractions for the same simulations, rising earlier and to higher levels than the no–jump control (labelled "1% jump, Antiviral"). Thick orange (dead) and thick cyan (antiviral) curves indicate IFN range 10 controls without free jumps; the orange curve peaks later (arrow, "Peak, no jump control") and at similar magnitude to the red curves, while the cyan curve shows a slower antiviral rise (labelled "No jump control"). The three insets (top right) show spatial patterns at $t = 120$ h: left, IFN range 1 with 1% free jumps yields scattered secondary plaques; middle, IFN range 10 with 1% free jumps forms larger but more contained plaques; right, IFN range 10 with no free jumps produces a single compact plaque. Inset colours: black, susceptible/uninfected; grey, dead; red, virus–infected; green, DIP–infected; yellow, co–infected; blue, antiviral. Simulation times reflect plaque expansion in an idealised *in vitro* epithelial monolayer.

https://doi.org/10.1371/journal.pcbi.1014198.g006

Increasing the IFN range provides stronger control: as the range grows, dead–cell peaks (red, orange) are reduced and delayed. The antiviral trajectories (blue, cyan), however, remain similar across ranges because their timing is largely set by τ . Thus, outcomes depend mainly on how many new foci are seeded outside the current IFN domain rather than on modest differences in IFN radius. Jumps that land beyond the front are particularly consequential, and DIPs tend to jump farther than viruses, increasing the likelihood of such events. Each new focus is rapidly encircled by antiviral cells and then declines, but repeated seeding during the delay accumulates damage.

Discussion

To our knowledge, there is no spatially explicit *in vitro* modelling framework that integrates DIPs and IFN responses. This work complements earlier lines of work: cellular automaton studies examined coinfection and plaque morphology in DIP–rich settings [9,28,30] but did not include IFN signalling, while ODE–based IFN models [22,25] captured timing and magnitude of responses but abstracted away spatial structure. We use this agent–based approach to bring these perspectives together by embedding DIP–IFN interactions in a spatial, stochastic framework. Our simulations are not intended to deliver precise predictions, but rather to generate mechanistic insights that can guide experimental design and future model refinement.

Building on this framework, we examined how spatial spread depends on IFN signalling and virus spread. We considered combinations of IFN spread (none, finite–range/local, global/instantaneous) and virus spread modes (cell–to–cell, finite–radius jumps, rare long–range jumps), under conditions with and without DIPs (Fig B in S1 Appendix).

As an initial validation, we calibrated the model to the conditions of *Baltes et al.* [33] to test qualitative consistency with the DIP–only dataset lacking IFN and to establish stochastic variability as a baseline for subsequent analyses. We also confirmed the IFN response dynamics by calibrating the model to the *Howat et al.* [26] dataset, which captures antiviral activation in MDBK and Vero cells under defined infection conditions. Together, these complementary datasets ensure that both spatial and immune aspects of the model are quantitatively grounded.

This experiment provides valuable insight into spatial spread in the presence of DIPs, but several key quantitative features are not available, especially data on the spatial extent of dead cells. Despite these constraints, our model reproduces the qualitative patterns: a virus–positive centre with ring–wise shifts in reporter dominance, patchy gene expression, and localised regions of DIP or coinfection enrichment, consistent with the concentric–ring analysis (Fig 2). Unlike *Liang et al.* [34], who analysed the same dataset with a partial differential equation (PDE) framework by dividing plaques into high– and low–density sectors, our agent–based model generates ring–like structures without imposed segmentation (Fig 2). This naturally patchy outcome arises because (i) we apply maximum–intensity projection, as in the experiment, so the initial red signal from lysed cells persists and maintains a virus–positive centre even after clearance, and (ii) in these experiments, DIPs disperse more broadly and stochastically in direction, leading virus–infected regions to remain red while later DIP infection produces more distant and patchy patterns. Additional example plots showing how relative DIP yield affects WT virion dynamics and infected-cell numbers are available in the Fig 5 GitHub folder. To help explore and interpret a broader range of viral infection phenomena, including those for which empirical data are becoming available, we provide a flexible RShiny app as an online platform designed to support such investigations.

We next analysed how IFN activation is regulated by relative DIP yield. In our implementation, coinfected cells were the strongest IFN producers (ten–fold above virus–only and roughly two–fold above DIP–only), and maximal IFN arose at an intermediate DIP yield that favoured broad DIP seeding followed by timely virus coinfection (Fig 5). At low DIP yield, coinfection was scarce and IFN remained modest; at high yield, early IFN curtailed further spread of both DIPs and viruses, limiting the cumulative number of secreting cells. Although our model represents within–cell replication indirectly, this pattern is consistent with reports that early replication kinetics shape the likelihood and timing of IFN induction [52]. We emphasise that “yield” here is a tissue–level control parameter rather than a direct surrogate for intracellular replication rate.

Spatial dispersal stands out in these analyses. Under local IFN signalling, finite–rate IFN was sufficient to halt infection when transmission was strictly local. However, introducing even a small fraction (~1%) of free–jump events allowed viruses and DIPs to escape IFN–dense zones and establish secondary plaques by seeding foci beyond the contemporaneous IFN front (Fig 6). These free jumps—potentially reflecting in vivo processes such as mucus–mediated transport or epithelial disruption—led to earlier and higher peaks in dead–cell fractions because IFN induction has a response delay τ , during which damage accumulates before local containment becomes effective. Increasing the IFN interaction range improved control by reducing the fraction of space left unprotected at any instant, but the timing of antiviral activation changed little, being largely set by τ . By contrast, under global or instantaneous IFN, the advantage of escaping local immune zones was lost, and free jumps had minimal impact. Although the precise dispersal behaviour of respiratory viruses *in vivo* remains uncertain, long–range, spatially discontinuous spread has been documented in murine models, such as inter–lobar transitions following low–dose inoculation [36]. This resemblance echoes the small–world effect, where the addition of just a few long–range connections can shorten path lengths in otherwise locally connected networks [53].

Finally, our results highlight a trade–off in IFN induction by DIPs. Too few DIPs allow wild–type virus to dominate, while too many suppress viral replication before IFN is strongly activated. At intermediate levels, IFN output is maximised, but the trade–off is not straightforward: strong local responses can be bypassed if viruses disperse by rare long–range jumps. Thus, IFN operates effectively only within the spatial domain it reaches, and additional IFN cannot prevent escape once particles move beyond that range. Together, these findings illustrate how DIPs enhance protection by balancing

containment and escape, suggesting design principles for therapies that aim to exploit or mimic DIP–induced immunity. More broadly, the balance we observe in our model may also shape virus evolution, as the interaction between DIPs, IFN, and dispersal determines which viral strategies can persist, though this balance may differ *in vivo* where additional biological complexity is present.

Beyond IAV, our model is flexible and adaptable to other pathogens, as DIPs are widely observed across viruses such as measles [54], SARS-CoV-2 [55], dengue [56], hepatitis B virus (HBV) [57], and HIV [58], etc. We also found that replacing the burst-style release model with a continuous Gaussian release model did not change our main conclusions: the intermediate optimum in IFN response and the qualitative long-range escape effect were both preserved (Figs E and F in S1 Appendix).

Caveats and model limitations

Limitations of the dataset. The experimental dataset from Baltes *et al.* [33], which includes DIPs but no IFN, provides a useful qualitative benchmark but omits key details such as the spatial extent and timing of cell death, natural monolayer gaps, and particle spreading ranges, all of which affect outcomes but cannot be fitted. Only four time points were imaged, further limiting temporal resolution. In Baltes *et al.* [33], separate red (virus) and green (DIP) channels were shown alongside merged images, but our attempts to digitally recombine the channels did not fully reproduce the published merge, likely due to resolution or processing differences not described in detail. This does not affect qualitative interpretation.

Qualitative nature of reporter measurements. The same dataset was also analysed by *Liang et al.* [34], who noted that reporter intensity is qualitative rather than quantitative. Thus, the images serve as indicators of viral gene expression but do not allow precise parameter calibration. While our simulations reproduce the main experimental features, the absence of dynamic measurements constrains time–resolved predictions. To address this, we also drew on data from *Howat et al.* [26], which include IFN but no DIPs, providing complementary context. As IFN responses can strongly alter spatial spreading dynamics, future studies should consider including clear imaging or other quantitative measurements of IFN diffusion rates and antiviral state transition times in DIP–infected systems, to better resolve DIP–IFN interactions.

Regulation of interferon production. A further complication is that IFN production is not a continuous process. Cells do not sustain secretion indefinitely; instead, expression is modulated by transcriptional feedback and other regulatory mechanisms [59]. Our current model does not include such downregulation, which may be important for understanding immune exhaustion and cytokine storm phenomena. In reality, IFN transcription can be switched off through repression, viral antagonism, or intrinsic negative feedback involving suppressor of cytokine signalling (SOCS) proteins, USP18, and PIAS1, generating temporal heterogeneity even among similarly infected cells. Immune signalling is further shaped by adaptive responses: $CD8^+$ T cells and B cells modulate IFN pathways, and their delayed engagement can influence plaque morphology and virus clearance *in vivo*. These layers of regulation, supported by recent studies [60], suggest that integrating transcriptional and cellular feedback into future models will improve biological realism and link innate with adaptive dynamics. In addition, the current model represents interferon signalling as a single effective antiviral response and focuses on type I IFN. The model does not distinguish between type I and type III interferons. Separating these pathways could improve biological realism and represents an interesting direction for future work.

Potential toxicity of high interferon levels. Our model does not include potential cytotoxic or pathological effects of high interferon levels. Excessive IFN responses may contribute to immunopathology, meaning that the peak IFN observed at intermediate DIP yields may not always correspond to a beneficial outcome for the host. Given the many roles of IFN, it is not clear what toxicity threshold would be appropriate for a given biological system, and determining such thresholds would likely require experimentation. For this reason, these effects were not incorporated into the present model. Future work could explore how IFN-associated toxicity might influence the relationship between DIP yield and IFN production.

Uncertainty in the location of the peak. Fig 5 shows that the highest IFN peak occurs at neither the minimum nor the maximum DIP level. However, the exact location of this peak depends on parameter choice, including burst size, the strength of intracellular competition between DIPs and virions, and related assumptions on progeny production. Because spatial data linking viruses, DIPs, and IFN are not yet available, this location cannot be fixed confidently in the present model. At the same time, non-spatial whole-host mouse data support the qualitative pattern that an intermediate DIP level gives the highest IFN peak [12]. These quantities remain poorly constrained for IAV and vary across strains and infected cells [41]. Therefore, the model supports the presence of an intermediate optimum, but not a precise value for where it occurs. More generally, the apparent IFN peak may become less pronounced depending on how particles are released over time (e.g., the width of the release-time distribution, controlled by sigma in the Gaussian release model; see Fig E in S1 Appendix).

Effects of interferon on epithelial repair. In addition, the present model assumes a constant epithelial regrowth rate and does not include the antiproliferative effects of interferon. IFN signalling can inhibit epithelial proliferation and delay tissue repair, which may influence recovery dynamics under high-IFN conditions.

Simplified representation of virus release and cell loss. Finally, the model represents virus production and cell loss as a single event. IAV virions are released by budding from the cell surface, and infected cells eventually lose viability as infection progresses. In the model, these processes are combined into a transition from the infected to the dead state, which captures the cumulative release of progeny during the intracellular infection cycle. A more detailed implementation that separates continuous budding from delayed cell death could refine the timing of virus release and would be a useful direction for future work.

Future directions

Future extensions of this model could further clarify how viral and immune processes interact. One improvement would be to introduce stochastic variation in IFN production across cells, capturing the heterogeneity observed in single–cell studies [61]. Another direction is to connect in vivo tissue–level dynamics to population–level spread using multi–scale modelling, which may clarify how DIPs shape transmission and immune control. While our study relies on stochastic simulations, their complexity can obscure mechanistic understanding. Analytical approximations or simplified models may help disentangle the nonlinear feedback processes underlying IFN responses.

From an experimental perspective, future studies should focus on quantifying IFN diffusion and antiviral state transition kinetics in cell culture systems coinfected with standard virus and DIPs.

In particular, experiments that distinguish between more temporally concentrated and more gradual particle release would help test which release formulation is more appropriate and whether release timing changes the location or shape of the IFN–yield relationship. Measuring and comparing the timing and abundance of co-infected cells in parallel would also be especially useful, as our results suggest that co-infection dynamics strongly shape the IFN response. Additional simulation replicates would also help determine whether fine-scale features of the IFN–yield curve are stable or reflect stochastic variation.

Although some *in vivo* data on DIP spreading are available [12], they typically provide only a few time points or lack spatial resolution. Time–lapse imaging combined with single–cell RNA sequencing could yield key data for refining model parameters, help explain experimental phenomena such as comet–like spread [62], and guide the design of future experiments. In addition, co–culture experiments with DIP–producing and non–DIP–producing viral strains would help validate the predicted effects of DIPs on infection dynamics and IFN responses.

Another important direction concerns the different mechanisms through which DIPs may control WT virus spread. DIPs can potentially limit WT virus infection through two routes: intracellular competition that slows WT virus replication within infected cells, and stimulation of interferon (IFN) responses that reduce the probability of infection in surrounding cells. Future work combining mathematical or computational modelling with experimental measurements

could help quantify the relative contribution of these two mechanisms and determine how their balance shapes infection dynamics.

Materials and methods

Because spatial infection data are essential for constraining our framework, we first calibrated the model against available experimental datasets. Full datasets that jointly track IFN and DIP dynamics are not yet available, but we can benchmark against published IFN-only and DIP-only experiments to capture complementary aspects of the system and ensure the model reproduces key qualitative features. Parameter values used to calibrate our model to the Baltes *et al.* data [33] (Figs 2 and 3), the Howat *et al.* data [26] (Fig 4), and to our own data are listed in Tables A–C in S1 Appendix.

Overall model structure

We start with a hexagonal lattice structure to represent the confluent epithelial monolayer, because epithelial cells adhere tightly during *in vitro* growth (Fig 1; [26,63]). This lattice–based, spatially explicit framework allows us to model individual cell interactions and capture the localised nature of infection, which cannot be approximated by homogeneous mixing or continuum diffusion models [64–67]. Cell connections are weighted by distance on the lattice, while the infection probabilities associated with these connections are updated hourly to capture the changing dynamics. The model defines seven cell states: susceptible, infected by both DIPs and viruses, infected by DIPs only, infected by viruses only, antiviral, dead, and regrowth (see Fig A in S1 Appendix for the schematic of model execution and explicit model transition rules). Simulations extend over several hundred hours to capture plaque expansion across the epithelial monolayer in vitro, rather than the duration of an acute influenza infection in a host.

Initial conditions

At the start of a simulation, all cells are susceptible. The standard grid size is 360 × 360 cells, matching the experimental field size in Howat et al. [26], while reduced 50 × 50 grids are used for small–scale tests. Viruses and DIPs are seeded by assigning initial particle counts to randomly selected cells, with $V_{PFU\_INITIAL} = 1$ and $D_{PFU\_INITIAL}$ varying by experimental condition.

Infection probability and IFN response

For A549 cells (which mount a robust IFN response to infection), the probability of infection for both viruses and DIPs is given by

$$P_{infection} = \rho \cdot \exp(-\alpha I),$$

where $\rho = 0.026$ as adapted from Howat et al. [26], I is the IFN concentration, and $\alpha = 1.5$ is the suppression factor. The IFN concentration is updated hourly under either local or global signalling.

Guided by experimental observations, we initialised simulations so that virus-only infected cells produce IFN at a baseline level, DIP-only infected cells produce approximately 5-fold more IFN than virus-only infected cells, and virus–DIP co-infected cells produce approximately 10-fold more IFN than virus-only infected cells. These fold differences reflect experimental observations that defective viral genomes are stronger activators of innate immune signalling [3,32]. The absolute IFN production rate can be adjusted in the online model interface.

In the model, infected cells begin producing IFN after a delay following infection. The IFN release time is drawn from a normal distribution with mean 5 h and standard deviation 1 h [68,69]. After this delay, each IFN-producing cell contributes to the total IFN concentration at every simulation step. The IFN concentration is updated according to

$$I(t + \Delta t) = I(t) + R \cdot N_{IFN} \cdot \Delta t,$$

where $I(t)$ is the IFN concentration at time t, N_{IFN} is the number of cells actively producing IFN, Δt is the simulation time step ($\Delta t = 1$ h in our simulations), and R is the IFN production rate per cell. IFN concentration is represented as a scaled variable rather than an absolute biochemical concentration, so the baseline IFN production rate is normalised to $R = 1$ IFN unit per cell per hour [26]. Different infected cell classes produce IFN at different relative rates. Virus-only infected cells produce IFN at the baseline rate ($R = 1$), DIP-only infected cells produce approximately five times more IFN ($5R = 5$), and virus–DIP co-infected cells produce approximately ten times more IFN ($10R = 10$). These fold differences reflect experimental observations that defective viral genomes can induce stronger innate immune signalling. The scale (fold-change) parameter values can be adjusted in the accompanying online app [3,32].

IFN induces an antiviral state in neighbouring cells after a mean delay of $\tau = 12$ h (standard deviation 3 h), with a half–life of 3 h [40,41]. Antiviral cells cannot be infected, creating local barriers to spread. In this setting, the virus is sensitive to the IFN response it provokes.

We implemented two distinct IFN signalling modes:

[1] **Finite–range/local signalling**, where IFN spreads diffusively over a limited radius, creating spatial gradients of protection. Under this mode, IFN secreted by infected cells influences neighbouring cells within a finite spatial radius on the hexagonal lattice. The IFN radius determines how far the antiviral signal spreads from each producing cell. This parameter is user-adjustable in the online model interface. In the default configuration used in the simulations presented here, the IFN interaction radius is set to 10 lattice units [70], meaning that IFN can influence all cells within ten lattice distances from the producing cell.

[2] **Global/instantaneous signalling**, where all cells share a uniform IFN concentration at each time step, corresponding to rapid homogenisation in well–mixed environments. For Vero cells (which lack an IFN response), $P_{infection} = \rho$ with all IFN–related parameters set to zero. Vero cells therefore remain susceptible throughout infection and never enter the antiviral state [26].

Infection cycle and particle release

In the default model, which we use as a simple baseline based on the available data and the calibration in Fig 4 [26], particle release is represented as a combined event that includes both budding over the infection period and burst-like release associated with infected-cell death; the corresponding results are shown in Figs 5 and 6.

Cells infected by viruses or co–infected progress to lysis after an average of 12 h (standard deviation 3 h), releasing progeny. Virus burst size follows a normal distribution with mean 50 PFU per cell, while DIP burst size averages 100 PFU per cell. DIP–only infected cells do not lyse but may convert to the antiviral state. Released particles disperse to neighbouring sites, with local particle density modulating the chance of successful entry.

In this default model, “cell death” represents the combined event of progeny release and subsequent cell death. Influenza virions are primarily released by budding from the cell surface, but infected cells ultimately undergo cell death. The model therefore represents this sequence as a single transition from the infected to the dead state, consistent with the base model tested on experimental data [26]; see Fig 4.

We also examined a continuous Gaussian release formulation, in which particle release is distributed over time; the corresponding results are shown in Figs E and F in S1 Appendix. In the Gaussian formulation, release is centred at $0.5T$ for each cell’s infection duration T, with standard deviation $0.25T$ (6.0 h and 3.0 h, respectively, for a mean lysis time of 12.0 h; details are given in the Supplementary Information). These values were used to represent gradual particle release over the infection period, to reflect reports that influenza virus budding occurs over several hours rather than as a single

instantaneous event [30,71]. Comparing these two formulations tests whether the main qualitative results depend on how particle release is distributed over time.

For intracellular competition, the DIP-to-virion ratio was defined for each infected cell from the numbers of extracellular DIPs and virions present at that cell at the time of entry. This entry ratio was then used to adjust progeny production at budding. Specifically, DIP amplification was scaled by the parameter dipReplicationAdvantage = 3.65 , based on [5], such that cells receiving a higher DIP-to-virion ratio produced fewer standard virions and more DIPs.

Cell lysis and regrowth

Cell regrowth occurs when a dead cell is adjacent to a healthy neighbour. Regrowth time follows a normal distribution with mean 24 h (standard deviation 6 h). Regrown cells revert to a susceptible state, allowing repeated infection.

In our framework, progeny particles released at lysis can spread in three distinct ways that mirror *in vitro* culture conditions: (i) **Cell–to–cell spread**, which approximates experiments where an agarose or methylcellulose overlay is applied to restrict particles to direct local contacts; (ii) **Finite–range dispersal**, where particles move over several cell diameters, modelling partial diffusion in semi–restricted environments; and (iii) **Unrestricted jumps**, where particles disperse freely across the culture dish without an overlay, as in standard liquid medium, allowing stochastic long–range seeding of secondary plaques.

Feedback dynamics

The cycle of infection, lysis, IFN release, antiviral conversion, cell death, and regrowth generates a feedback loop that drives complex spatial and temporal infection dynamics. This structure provides the foundation for model calibration and experimental comparison described in results.

Supporting information

S1 Appendix. Fig A. Model execution flowchart and explicit transition rules. The simulation begins by setting up a hexagonal grid where all cells are initially susceptible. Viruses and DIPs are introduced based on the inoculum size. Infection dynamics unfold through stochastic transitions: susceptible and regrowth cells become infected based on local particle and IFN levels. Infected cells undergo lysis, release particles and IFN, and die (for IAV, virus release occurs by budding rather than lysis, but infected cells ultimately die from infection; the simulation outcome is therefore equivalent). Dead cells regrow if healthy neighbours are present. The model continues until termination criteria are met. Output includes time–resolved data and spatial maps. Animations available at: https://shiny-spatial-infection-app-production.up.railway.app/. **Fig B. Dynamics of spread under varying particle–jump behaviours and IFN conditions.** Outcomes are shown for scenarios with both DIPs and viruses (top three rows) and viruses only (bottom three rows), under three movement modes: cell–to–cell (left column), finite–radius jumps (middle column), and random jumps (right column). Each row corresponds to a different IFN mode: no IFN, finite–range IFN spread, and global/instantaneous IFN spread. Left plot: temporal dynamics on a $\log_{10}$ scale showing the percentage of cells in each state and global IFN concentration per cell. Right plot: the final spatial distribution of states. **Fig C. Heterogeneity in infection dynamics and plaque morphology under varying proportions of cell–to–cell and free–jump spread in Vero cells.** Left panels: line plots illustrating the percentage of infected cells over time. Right panels: final plaque morphology at the simulation endpoint ($t = 300$ hours). Bottom panels: plaque development over time at $t = 50$, 100, 150, and 200 hours. **Fig D. Comparison of plaque dynamics under global IFN with 1% free–jump transmission, in the absence (left) and presence (right) of DIPs.** Top panels: time courses showing percentages of antiviral cells, virus–infected cells, DIP–infected cells, and co–infected cells. Bottom panels: representative spatial snapshots at $t = 50$, 100, 150, and 200 hours, illustrating how DIPs promote co–infection and more diffuse plaque morphology despite similar levels of antiviral activation. **Fig E. IFN dynamics across**

values of the relative DIP yield under continuous Gaussian release of progeny particles. Left: IFN time series for increasing relative DIP yield; the highest IFN peak still occurred at an intermediate relative DIP yield. Right: peak IFN as a function of relative DIP yield across stochastic replicates, with GAM and LOESS fits recovering an interior maximum. **Fig F. IFN range and spreading mode jointly shape plaque dynamics under continuous Gaussian release of progeny particles.** Even a small fraction of free jumps led to earlier accumulation of dead cells despite stronger antiviral activation, showing that long–range dispersal could still escape local IFN control when particle release was distributed continuously through time. **Table A. Parameters corresponding to Figs 2 and 3. Table B. Parameters corresponding to Fig 4. Table C. Parameters for the base model simulation.**
(PDF)

Acknowledgments

All authors gave final approval for publication and agreed to be held accountable for the work performed therein.

Ethics statement: This study did not involve human participants or animals. Ethical approval was not required.

Use of Artificial Intelligence (AI)-assisted technologies: AI-assistance was used for grammar correction and completing lines in our code. All AI-produced code and information were verified by Yimei Li.

Author contributions

Conceptualization: Yimei Li.

Formal analysis: Yimei Li, Bjarke Frost Nielsen, Aartjan te Velthuis, Bryan T. Grenfell.

Funding acquisition: Bjarke Frost Nielsen, Simon A. Levin, Aartjan te Velthuis, Bryan T. Grenfell.

Methodology: Yimei Li, Aartjan te Velthuis.

Software: Yimei Li, Bjarke Frost Nielsen, Aartjan te Velthuis, Bryan T. Grenfell.

Supervision: Aartjan te Velthuis.

Validation: Yimei Li, Bjarke Frost Nielsen, Aartjan te Velthuis, Bryan T. Grenfell.

Visualization: Yimei Li.

Writing – original draft: Yimei Li.

Writing – review & editing: Yimei Li, Bjarke Frost Nielsen, Simon A. Levin, Aartjan te Velthuis, Bryan T. Grenfell.

References

1. Von Magnus P. Advances in Virus Research. Elsevier. 1954. 59–79. https://doi.org/10.1016/S0065-3527(08)60529-1
2. Huang AS, Baltimore D. Defective viral particles and viral disease processes. Nature. 1970;226(5243):325–7. https://doi.org/10.1038/226325a0 PMID: 5439728
3. Vignuzzi M, López CB. Defective viral genomes are key drivers of the virus-host interaction. Nat Microbiol. 2019;4(7):1075–87. https://doi.org/10.1038/s41564-019-0465-y PMID: 31160826
4. Karki B, Bull JJ, Krone SM. Modeling the therapeutic potential of defective interfering particles in the presence of immunity. Virus Evol. 2022;8(2):veac047. https://doi.org/10.1093/ve/veac047 PMID: 35799886
5. Laske T, Heldt FS, Hoffmann H, Frensing T, Reichl U. Modeling the intracellular replication of influenza A virus in the presence of defective interfering RNAs. Virus Res. 2016;213:90–9. https://doi.org/10.1016/j.virusres.2015.11.016 PMID: 26592173
6. Ranum JN, Ledwith MP, Alnaji FG, Diefenbacher M, Orton R, Sloan E, et al. Cryptic proteins translated from deletion-containing viral genomes dramatically expand the influenza virus proteome. Nucleic Acids Res. 2024;52(6):3199–212. https://doi.org/10.1093/nar/gkae133 PMID: 38407436
7. Saira K, Lin X, DePasse JV, Halpin R, Twaddle A, Stockwell T, et al. Sequence analysis of in vivo defective interfering-like RNA of influenza A H1N1 pandemic virus. J Virol. 2013;87(14):8064–74. https://doi.org/10.1128/JVI.00240-13 PMID: 23678180
8. Ke R, Aaskov J, Holmes EC, Lloyd-Smith JO. Phylodynamic analysis of the emergence and epidemiological impact of transmissible defective dengue viruses. PLoS Pathog. 2013;9(2):e1003193. https://doi.org/10.1371/journal.ppat.1003193 PMID: 23468631

9. Akpinar F, Inankur B, Yin J. Spatial-Temporal Patterns of Viral Amplification and Interference Initiated by a Single Infected Cell. J Virol. 2016;90(16):7552–66. https://doi.org/10.1128/JVI.00807-16 PMID: 27279621
10. Vasilijevic J, Zamarreño N, Oliveros JC, Rodriguez-Frandsen A, Gómez G, Rodriguez G, et al. Reduced accumulation of defective viral genomes contributes to severe outcome in influenza virus infected patients. PLoS Pathog. 2017;13(10):e1006650. https://doi.org/10.1371/journal.ppat.1006650 PMID: 29023600
11. Felt SA, Sun Y, Jozwik A, Paras A, Habibi MS, Nickle D, et al. Detection of respiratory syncytial virus defective genomes in nasal secretions is associated with distinct clinical outcomes. Nat Microbiol. 2021;6(5):672–81. https://doi.org/10.1038/s41564-021-00882-3 PMID: 33795879
12. Penn R, Tregoning JS, Flight KE, Baillon L, Frise R, Goldhill DH, et al. Levels of Influenza A Virus Defective Viral Genomes Determine Pathogenesis in the BALB/c Mouse Model. J Virol. 2022;96(21):e0117822. https://doi.org/10.1128/jvi.01178-22 PMID: 36226985
13. Ghorbani A, Ngunjiri JM, Rendon G, Brooke CB, Kenney SP, Lee C-W. Diversity and Complexity of Internally Deleted Viral Genomes in Influenza A Virus Subpopulations with Enhanced Interferon-Inducing Phenotypes. Viruses. 2023;15(10):2107. https://doi.org/10.3390/v15102107 PMID: 37896883
14. Te Velthuis AJW, Long JC, Bauer DLV, Fan RLY, Yen H-L, Sharps J, et al. Mini viral RNAs act as innate immune agonists during influenza virus infection. Nat Microbiol. 2018;3(11):1234–42. https://doi.org/10.1038/s41564-018-0240-5 PMID: 30224800
15. Pitré E, Bisht K, Remick KA, Ghorbani A, Yewdell JW, Elshina E, et al. A two-step mechanism for RIG-I activation by influenza virus mvRNAs. Sci Adv. 2025;11(32):eadw8034. https://doi.org/10.1126/sciadv.adw8034 PMID: 40779639
16. Wu M, Zhou E, Sheng R, Fu X, Li J, Jiang C. Defective interfering particles of influenza virus and their characteristics, impacts, and use in vaccines and antiviral strategies: a systematic review. Viruses. 2022;14(12):2773. https://doi.org/10.3390/v14122773
17. Gould PS, Easton AJ, Dimmock NJ. Live Attenuated Influenza Vaccine contains Substantial and Unexpected Amounts of Defective Viral Genomic RNA. Viruses. 2017;9(10):269. https://doi.org/10.3390/v9100269 PMID: 28934167
18. Bellocq C, Mottet G, Roux L. Wide occurrence of measles virus subgenomic RNAs in attenuated live-virus vaccines. Biologicals. 1990;18(4):337–43. https://doi.org/10.1016/1045-1056(90)90039-3 PMID: 2285505
19. Derdeyn CA, Frey TK. Characterization of defective-interfering RNAs of rubella virus generated during serial undiluted passage. Virology. 1995;206(1):216–26. https://doi.org/10.1016/s0042-6822(95)80036-0 PMID: 7831776
20. Bora M, Manu M, Karki M. Exploring the mechanisms of interference, persistence and antiviral potential of defective interfering particles. Discov Viruses. 2025;2(1). https://doi.org/10.1007/s44370-025-00007-y
21. Brennan JW, Sun Y. Defective viral genomes: Advances in understanding their generation, function, and impact on infection outcomes. mBio. 2024;15(5):e0069224. https://doi.org/10.1128/mbio.00692-24
22. Baccam P, Beauchemin C, Macken CA, Hayden FG, Perelson AS. Kinetics of influenza A virus infection in humans. J Virol. 2006;80(15):7590–9. https://doi.org/10.1128/JVI.01623-05 PMID: 16840338
23. Saenz RA, Quinlivan M, Elton D, Macrae S, Blunden AS, Mumford JA, et al. Dynamics of influenza virus infection and pathology. J Virol. 2010;84(8):3974–83. https://doi.org/10.1128/JVI.02078-09 PMID: 20130053
24. Pawelek KA, Huynh GT, Quinlivan M, Cullinane A, Rong L, Perelson AS. Modeling within-host dynamics of influenza virus infection including immune responses. PLoS Comput Biol. 2012;8(6):e1002588. https://doi.org/10.1371/journal.pcbi.1002588 PMID: 22761567
25. Murillo LN, Murillo MS, Perelson AS. Towards multiscale modeling of influenza infection. J Theor Biol. 2013;332:267–90. https://doi.org/10.1016/j.jtbi.2013.03.024 PMID: 23608630
26. Howat TJ, Barreca C, O'Hare P, Gog JR, Grenfell BT. Modelling dynamics of the type I interferon response to in vitro viral infection. J R Soc Interface. 2006;3(10):699–709. https://doi.org/10.1098/rsif.2006.0136 PMID: 16971338
27. Ivashkiv LB, Donlin LT. Regulation of type I interferon responses. Nat Rev Immunol. 2014;14(1):36–49. https://doi.org/10.1038/nri3581 PMID: 24362405
28. Rüdiger D, Pelz L, Hein MD, Kupke SY, Reichl U. Multiscale model of defective interfering particle replication for influenza A virus infection in animal cell culture. PLoS Comput Biol. 2021;17(9):e1009357. https://doi.org/10.1371/journal.pcbi.1009357 PMID: 34491996
29. Kirkwood TB, Bangham CR. Cycles, chaos, and evolution in virus cultures: a model of defective interfering particles. Proc Natl Acad Sci U S A. 1994;91(18):8685–9. https://doi.org/10.1073/pnas.91.18.8685 PMID: 8078942
30. Frensing T, Heldt FS, Pflugmacher A, Behrendt I, Jordan I, Flockerzi D, et al. Continuous influenza virus production in cell culture shows a periodic accumulation of defective interfering particles. PLoS One. 2013;8(9):e72288. https://doi.org/10.1371/journal.pone.0072288 PMID: 24039749
31. Liao LE, Iwami S, Beauchemin CAA. (In)validating experimentally derived knowledge about influenza A defective interfering particles. J R Soc Interface. 2016;13(124):20160412. https://doi.org/10.1098/rsif.2016.0412 PMID: 27881801
32. Tapia K, Kim W-K, Sun Y, Mercado-López X, Dunay E, Wise M, et al. Defective viral genomes arising in vivo provide critical danger signals for the triggering of lung antiviral immunity. PLoS Pathog. 2013;9(10):e1003703. https://doi.org/10.1371/journal.ppat.1003703 PMID: 24204261
33. Baltes A, Akpinar F, Inankur B, Yin J. Inhibition of infection spread by co-transmitted defective interfering particles. PLoS One. 2017;12(9):e0184029. https://doi.org/10.1371/journal.pone.0184029 PMID: 28915264
34. Liang Q, Yang J, Fan W-TL, Lo W-C. Patch formation driven by stochastic effects of interaction between viruses and defective interfering particles. PLoS Comput Biol. 2023;19(10):e1011513. https://doi.org/10.1371/journal.pcbi.1011513 PMID: 37782667

35. Bals R, Hiemstra PS. Innate immunity in the lung: how epithelial cells fight against respiratory pathogens. Eur Respir J. 2004;23(2):327–33. https://doi.org/10.1183/09031936.03.00098803 PMID: 14979512
36. Tran V, Moser LA, Poole DS, Mehle A. Highly sensitive real-time in vivo imaging of an influenza reporter virus reveals dynamics of replication and spread. J Virol. 2013;87(24):13321–9. https://doi.org/10.1128/JVI.02381-13 PMID: 24089552
37. Manicassamy B, Manicassamy S, Belicha-Villanueva A, Pisanelli G, Pulendran B, García-Sastre A. Analysis of in vivo dynamics of influenza virus infection in mice using a GFP reporter virus. Proc Natl Acad Sci U S A. 2010;107(25):11531–6. https://doi.org/10.1073/pnas.0914994107 PMID: 20534532
38. Cangelosi Q, Means SA, Ho H. A multi-scale spatial model of hepatitis-B viral dynamics. PLoS One. 2017;12(12):e0188209. https://doi.org/10.1371/journal.pone.0188209 PMID: 29216213
39. Park AW, Daly JM, Lewis NS, Smith DJ, Wood JLN, Grenfell BT. Quantifying the impact of immune escape on transmission dynamics of influenza. Science. 2009;326(5953):726–8. https://doi.org/10.1126/science.1175980 PMID: 19900931
40. Elshina E. Investigating the mechanisms behind the immunostimulatory activity of influenza A virus RNA polymerase mutations. University of Cambridge. 2022. https://www.repository.cam.ac.uk/handle/1810/352749
41. Zath GK, Thomas MM, Loveday EK, Bikos DA, Sanche S, Ke R, et al. Influenza A viral burst size from thousands of infected single cells using droplet quantitative PCR (dqPCR). PLoS Pathog. 2024;20(7):e1012257. https://doi.org/10.1371/journal.ppat.1012257 PMID: 38950082
42. Alnaji FG, Reiser WK, Rivera-Cardona J, Te Velthuis AJW, Brooke CB. Influenza A Virus Defective Viral Genomes Are Inefficiently Packaged into Virions Relative to Wild-Type Genomic RNAs. mBio. 2021;12(6):e0295921. https://doi.org/10.1128/mBio.02959-21 PMID: 34809454
43. Hutchinson EC, Curran MD, Read EK, Gog JR, Digard P. Mutational analysis of cis-acting RNA signals in segment 7 of influenza A virus. J Virol. 2008;82(23):11869–79. https://doi.org/10.1128/JVI.01634-08 PMID: 18815307
44. Davis AR, Nayak DP. Sequence relationships among defective interfering influenza viral RNAs. Proc Natl Acad Sci U S A. 1979;76(7):3092–6. https://doi.org/10.1073/pnas.76.7.3092 PMID: 290988
45. Peterl S, Lahr CM, Schneider CN, Meyer J, Podlipensky X, Lechner V, et al. Morphology-dependent entry kinetics and spread of influenza A virus. EMBO J. 2025;44(14):3959–82. https://doi.org/10.1038/s44318-025-00481-6 PMID: 40490555
46. Rampling R, Cruickshank G, Papanastassiou V, Nicoll J, Hadley D, Brennan D, et al. Toxicity evaluation of replication-competent herpes simplex virus (ICP 34.5 null mutant 1716) in patients with recurrent malignant glioma. Gene Ther. 2000;7(10):859–66. https://doi.org/10.1038/sj.gt.3301184 PMID: 10845724
47. Desmyter J, Melnick JL, Rawls WE. Defectiveness of interferon production and of rubella virus interference in a line of African green monkey kidney cells (Vero). J Virol. 1968;2(10):955–61. https://doi.org/10.1128/JVI.2.10.955-961.1968 PMID: 4302013
48. Rhim JS, Schell K, Creasy B, Case W. Biological characteristics and viral susceptibility of an African green monkey kidney cell line (Vero). Proc Soc Exp Biol Med. 1969;132(2):670–8. https://doi.org/10.3181/00379727-132-34285 PMID: 4982209
49. Emeny JM, Morgan MJ. Regulation of the interferon system: evidence that Vero cells have a genetic defect in interferon production. J Gen Virol. 1979;43(1):247–52. https://doi.org/10.1099/0022-1317-43-1-247 PMID: 113494
50. Barreca C, O'Hare P. Suppression of herpes simplex virus 1 in MDBK cells via the interferon pathway. J Virol. 2004;78(16):8641–53. https://doi.org/10.1128/JVI.78.16.8641-8653.2004 PMID: 15280473
51. Härle P, Sainz B, Carr DJJ, Halford WP. The immediate-early protein, ICP0, is essential for the resistance of herpes simplex virus to interferon-α/β. Virology. 2002;293(2):295–304. https://doi.org/10.1006/viro.2001.1280
52. Bruurs LJM, Müller M, Schipper JG, Rabouw HH, Boersma S, van Kuppeveld FJM, et al. Antiviral responses are shaped by heterogeneity in viral replication dynamics. Nat Microbiol. 2023;8(11):2115–29. https://doi.org/10.1038/s41564-023-01501-z PMID: 37814072
53. Watts DJ, Strogatz SH. Nature. 1998;393(6684):440–2. https://doi.org/10.1038/30918
54. Rima BK, Davidson WB, Martin SJ. The role of defective interfering particles in persistent infection of Vero cells by measles virus. J Gen Virol. 1977;35(1):89–97. https://doi.org/10.1099/0022-1317-35-1-89 PMID: 404394
55. Kalamvoki M, Norris V. A Defective Viral Particle Approach to COVID-19. Cells. 2022;11(2):302. https://doi.org/10.3390/cells11020302 PMID: 35053418
56. Li D, Lin M-H, Rawle DJ, Jin H, Wu Z, Wang L, et al. Dengue virus-free defective interfering particles have potent and broad anti-dengue virus activity. Commun Biol. 2021;4(1):557. https://doi.org/10.1038/s42003-021-02064-7 PMID: 33976375
57. Yuan TT, Lin MH, Chen DS, Shih C. A defective interference-like phenomenon of human hepatitis B virus in chronic carriers. J Virol. 1998;72(1):578–84. https://doi.org/10.1128/JVI.72.1.578-584.1998 PMID: 9420261
58. Nelson GW, Perelson AS. Modeling defective interfering virus therapy for AIDS: conditions for DIV survival. Math Biosci. 1995;125(2):127–53. https://doi.org/10.1016/0025-5564(94)00021-q PMID: 7881191
59. Hiscott J, Grandvaux N, Sharma S, Tenoever BR, Servant MJ, Lin R. Convergence of the NF-κB and interferon signaling pathways in the regulation of antiviral defense and apoptosis. Ann N Y Acad Sci. 2003;1010:237–48. https://doi.org/10.1196/annals.1299.042 PMID: 15033728
60. Centofanti E, Wang C, Iyer S, Krichevsky O, Oyler-Yaniv A, Oyler-Yaniv J. The spread of interferon-γ in melanomas is highly spatially confined, driving nongenetic variability in tumor cells. Proc Natl Acad Sci U S A. 2023;120(35):e2304190120. https://doi.org/10.1073/pnas.2304190120 PMID: 37603742

61. Rand U, Rinas M, Schwerk J, Nöhren G, Linnes M, Kröger A, et al. Multi-layered stochasticity and paracrine signal propagation shape the type-I interferon response. Mol Syst Biol. 2012;8:584. https://doi.org/10.1038/msb.2012.17 PMID: 22617958
62. Lindsay SM, Timm A, Yin J. A quantitative comet infection assay for influenza virus. J Virol Methods. 2012;179(2):351–8. https://doi.org/10.1016/j.jviromet.2011.11.022
63. Nagai T, Honda H. A dynamic cell model for the formation of epithelial tissues. Philosophical Magazine B. 2001;81(7):699–719. https://doi.org/10.1080/13642810108205772
64. Cohen DS, Murray JD. A generalized diffusion model for growth and dispersal in a population. J Math Biology. 1981;12(2):237–49. https://doi.org/10.1007/bf00276132
65. Murray JD. Mathematical Biology. 1st ed. Springer. 1989. https://doi.org/10.1007/978-3-662-08539-4
66. Fearon DT, Locksley RM. The instructive role of innate immunity in the acquired immune response. Science. 1996;272(5258):50–3. https://doi.org/10.1126/science.272.5258.50 PMID: 8600536
67. Gatenby RA, Gawlinski ET. A reaction-diffusion model of cancer invasion. Cancer Res. 1996;56(24):5745–53. PMID: 8971186
68. Marcus PI, Rojek JM, Sekellick MJ. Interferon induction and/or production and its suppression by influenza A viruses. J Virol. 2005;79(5):2880–90. https://doi.org/10.1128/JVI.79.5.2880-2890.2005 PMID: 15709007
69. Zhai B, Liu L, Li X, Lv X, Wu J, Li J, et al. The Variation of Duck RIG-I-Mediated Innate Immune Response Induced by Different Virulence Avian Influenza Viruses. Front Microbiol. 2022;13:842721. https://doi.org/10.3389/fmicb.2022.842721 PMID: 35300481
70. Aponte-Serrano JO, Weaver JJA, Sego TJ, Glazier JA, Shoemaker JE. Multicellular spatial model of RNA virus replication and interferon responses reveals factors controlling plaque growth dynamics. PLoS Comput Biol. 2021;17(10):e1008874. https://doi.org/10.1371/journal.pcbi.1008874 PMID: 34695114
71. Heldt F. Mathematical models of influenza A virus infection: from intracellular replication to virus growth in cell populations. 2015.